

Wetting on the Microscale: Shape of a Liquid Drop on a Microstructured Surface at Different Length Scales

Periklis Papadopoulos, Xu Deng, Lena Mammen, Dirk-Michael Drotlef, Glauco Battagliarin, Chen Li, Klaus Müllen, Katharina Landfester, Aranzazu del Campo, Hans-Jürgen Butt, and Doris Vollmer*

2012, 28 (22), 8392–8398. DOI: 10.1021/la300379u

The color of the figures in the original article has been corrected, and the figures are reposted below, starting with the table of contents/abstract graphic.

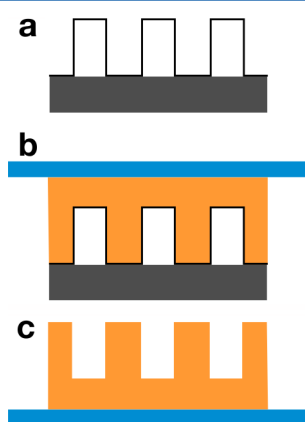


Figure 1. Sketch of the fabrication of cylindrical PDMS pillars. (a) A SU-8 photoresist patterned wafer with cylindrical holes was used as template. (b) A 10:1 ratio of PDMS prepolymer and cross-linker (Sylgard 184, Dow Corning) labeled with the hydrophobic PMI dye was poured on the template. Care was taken that the thickness of the PDMS film did not exceed 30 μm . Excess material is allowed to drain slowly. Finally, a thin (140 μm) glass slide is placed on the PDMS film (blue). (c) After the PDMS film is cured at 100 $^{\circ}\text{C}$ for 1 h the glass slide is removed slowly, so that the square lattice of cylindrical pillars remains undamaged on the glass slide. The total thickness is about 170 μm .

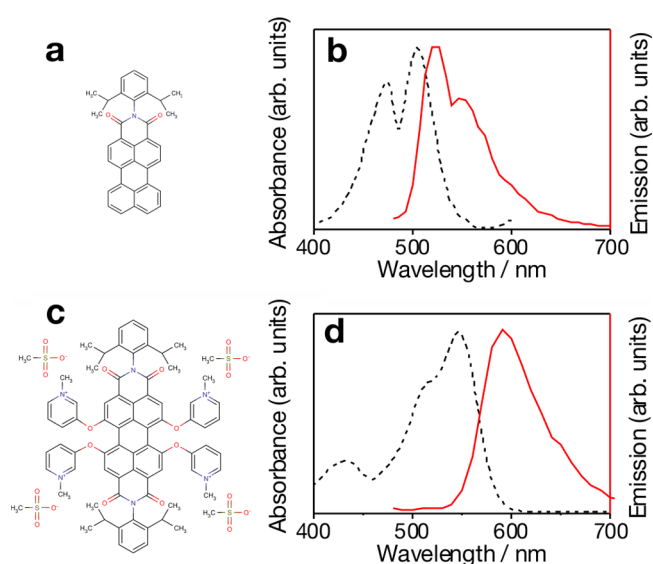


Figure 2. (a) Hydrophobic *N*-(2,6-diisopropylphenyl)-3,4-perylenedicarboxylic acid monoimide (PMI) dye, used for labeling the PDMS substrate. (b) Absorption (dashed black) and fluorescence (solid red) spectra of PMI. Both spectra were measured in a PDMS film containing PMI at a concentration of 0.05 mg/mL. The absorption shows a maximum around 505 nm, whereas the emission maximum is around 525 nm. The absorption spectrum is measured with a Perkin-Elmer UV–vis spectrometer and the emission with the Leica TCS SP5 II confocal microscope by varying the spectral range in steps of 5 nm. (c) Chemical structure of *N,N'*-(2,6-diisopropylphenyl)-1,6,7,12-tetra(1-methylpyridinium-3-yloxy)perylene-3,4,9,10-tetracarboxylic acid diimide tetramethanesulfonate (WS-PDI). This hydrophilic dye was used to label the water phase. (d). Absorption (black) and fluorescence (red) of WS-PDI. The spectra are obtained from a 0.05 mg/mL water solution of WS-PDI. The absorption and emission maxima are 545 and 590 nm, respectively.

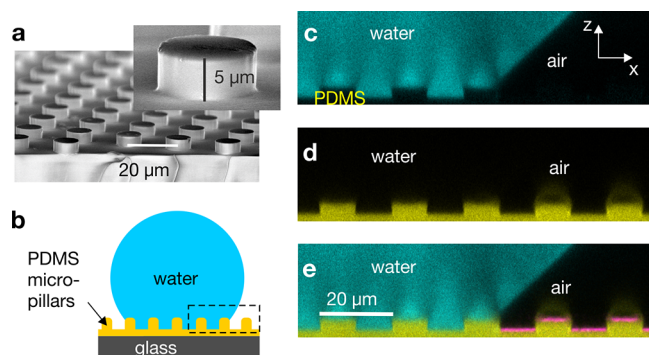


Figure 3. Fluorescently labeled substrate and water drops. (a) Scanning electron microscope image of a square lattice of cylindrical PDMS pillars, prepared by soft-molding. Inset: magnification of a single pillar. The root-mean-square roughness (rms) on top of and in between the pillars was determined by AFM on an area of $1 \times 1 \mu\text{m}^2$ and calculated to be 5 ± 2 nm. SEM images were taken without modifying the pillars' surface. (b) Schematic side view of a water droplet placed on the pillar array. (c) Fluorescence image of a section of a water droplet dyed with WS-PDI in contact with PDMS pillars and air. The PDMS substrate is labeled with PMI and is not visible because the wavelengths of PMI and WS-PDI are well separated. (d) Fluorescence image of a section of a dyed PDMS microstructured substrate. (e) Superposition of the simultaneously recorded confocal images of water (cyan), PDMS (yellow), and light reflected at the PDMS–air interface (magenta).

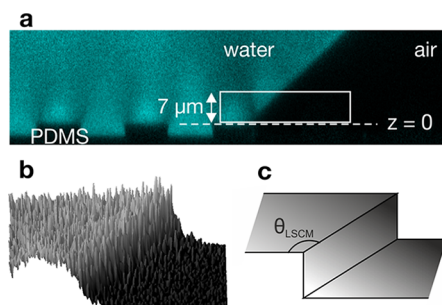


Figure 4. Fitting of the contact angle θ_{LSCM} , as defined in the text. (a) The fluorescence image (Figure 3c) is corrected for attenuation due to spherical aberration (dry objective, dye in water), by normalizing the intensity of each line. Areas of about $7 \mu\text{m}$ high and $50 \mu\text{m}$ width are taken to calculate the contact angle “on the pillars”. Heights z are measured with respect to the plane at the top of pillars (dashed line). (b) 3D representation of the intensity of the selected part. The intensity of the pixels is plotted as height. (c) The selection is fitted with a 2D step function with arbitrary boundaries.

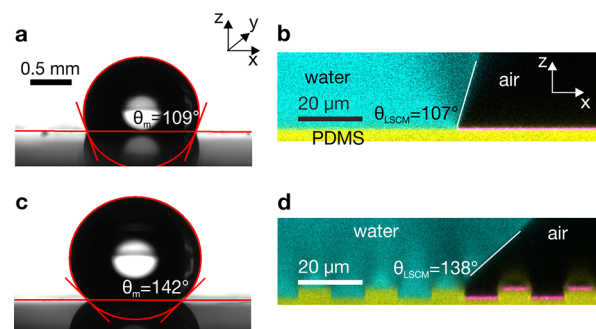


Figure 5. Contact angles at different length scales. (a) Static contact angle of water drops ($\sim 10 \mu\text{L}$) on a flat PDMS surface measured by optical microscopy, θ_m , and (b) LSCM, θ_{LSCM} . (c, d) Respective images for a water drop on a PDMS pillar square. The drop profile in the xz -plane is analyzed to obtain θ_{LSCM} (Figure 4).

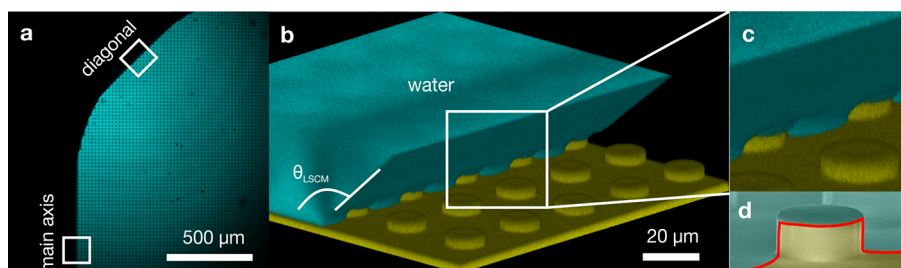


Figure 6. 3D images of a sessile water drop on a square lattice of PDMS pillars. (a) Horizontal section (10 \times) of a fluorescently labeled sessile water drop just above the pillars. The drop is preferably pinned along the main axes and the diagonal of the square lattice. (b) 3D image (40 \times) of a section of the drop, showing pinning along the main axis of a PDMS pillar square lattice. This section is indicated with a white square in (a). The angle θ_{LSCM} is marked. (c) Magnified section of (b) showing the varying curvature of the water–air interface. (d) Contact line of a wetted pillar (red line). The gray part is wetted with water; the yellow region is in contact with air.

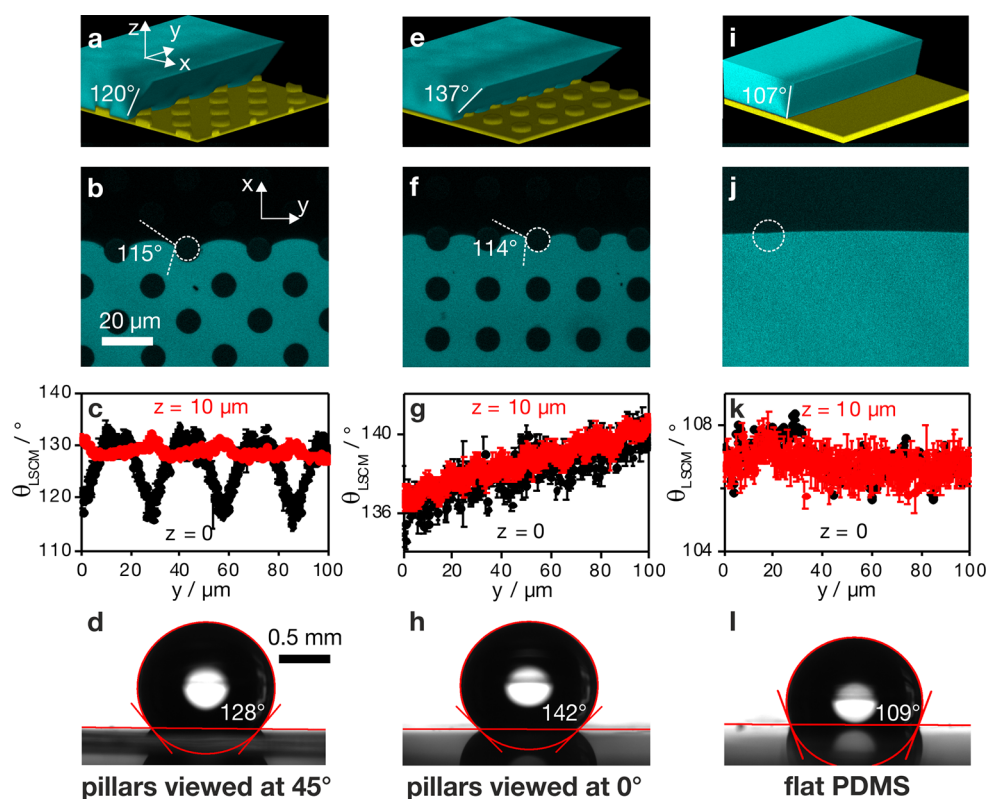


Figure 7. Variation of θ_{LSCM} along the contact line. (a–h) Contact lines and angles (θ_{LSCM}) of water drops deposited on a microstructured substrate and (i–l) on flat PDMS. (a) Section of a 3D fluorescence image, where a drop is pinned along the diagonal of the lattice (Figure 6a). The value of θ_{LSCM} at $y = 0$ and $z = 0$ is added. (b) Horizontal (xy) cross section of the water air interface at the bottom of the substrate ($z = -5 \mu\text{m}$). The contact angle at the pillars' side is indicated (white circle). (c) Variation of the respective contact angle θ_{LSCM} along the contact line, evaluated at $z = 0$ (black points) and $z = 10 \mu\text{m}$ (red points). (d) Macroscopic contact angle measured by optical microscopy. The drop is viewed at 45° with respect to the lattice. (e) The same drop is pinned along the square lattice main axis (Figure 6a). (f) Respective xy cross section ($z = -5 \mu\text{m}$), (g) contact angle values, and (h) optical microscopy image at 0° . (i–l) Respective images for a drop on a flat pillar lattice. The volume of the drop on the PDMS substrate was about $30 \mu\text{L}$. In all other cases drop volume was about $15 \mu\text{L}$. The length scale in each row is fixed.

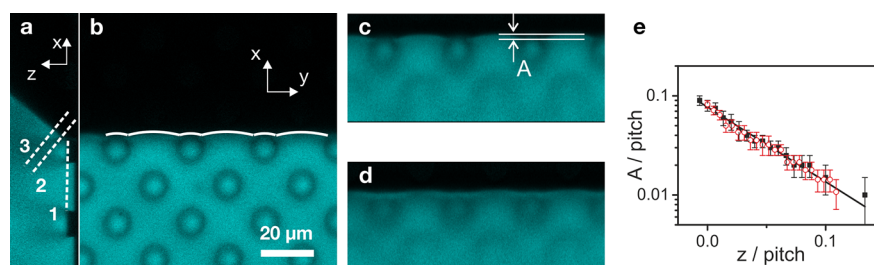


Figure 8. Water drop on a microstructured surface. (a) Vertical (xz) section of the drop along the part of the contact line pinned at 45° (Figure 6a). (b) Horizontal (xy) section on top of the pillars ($z = 0$), denoted by “1” in (a). The white line shows the curvature on and between the pillars. (c) Section normal to the water–air interface at the top of the pillars, denoted by “2” in (a). The peak-to-peak amplitude of the deviation from the plane is denoted by A . (d) Similar section $2\ \mu\text{m}$ higher in the z -direction, denoted by “3” in (a). (e) Scaled peak-to-peak deviation amplitude A/P as a function of scaled height z/P . The contact line is pinned at 0° (black points) or 45° (red points), and the respective pitch P is 20 and $28\ \mu\text{m}$ (Figure 6a). The black line is a fit with exponential decay.

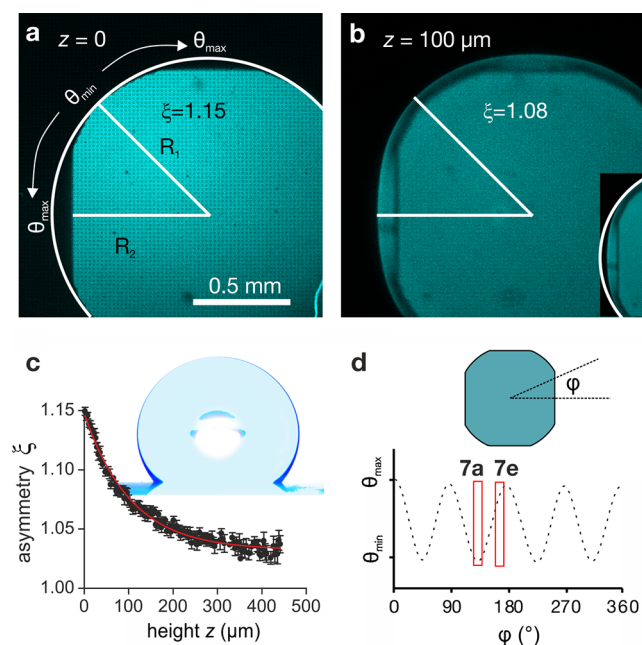


Figure 9. Variation of 2D horizontal cross sections ($10\times$) of a water drop ($15\ \mu\text{L}$) with increasing vertical distance z from the microstructured substrate. (a) Just above the substrate ($z = 0$). The asymmetry of the contact line, ξ , is defined as the ratio of radius R_1 to the shortest distance from the center R_2 , $\xi = R_1/R_2$. The contact angle took its minimum value, θ_{\min} , at the center of the diagonal and its maximum value, θ_{\max} , at the center of the main axis. (b) With increasing distance z from the substrate the asymmetry of the contact line decreased, until finally, the water cross section became almost circular. (c) Asymmetry factor, ξ , of horizontal cross sections through a drop, calculated at different distance to the substrate. An exponential fit is indicated by the red line. Inset: superposition of an image of a drop taken by optical microscopy along the main axis (cyan) and diagonal (blue), showing that the asymmetry persisted well above the surface. (d) Sketch of the variation of the macroscopic contact angle along the contact line. These large-scale variations need to be distinguished from the local variations of the contact angle, caused by the shape of a single pillar and the pillar–pillar distance (e.g., Figure 7c). The red rectangles show the measurement ranges in Figures 7a–d and 7e–h, respectively. The latter is deliberately slightly off the maximum.